

CONSTITUTIVE MODELS FOR STRONGLY CURVED BEAMS IN THE FRAME OF ISOGEOMETRIC ANALYSIS

ANTONIO CAZZANI, MARCELLO MALAGÙ, FLAVIO STOCHINO, AND EMILIO TURCO

ABSTRACT. The current development of isogeometric approach in various fields of Mechanics is explained by the high accuracy results which can be achieved at a reduced computational cost by codes based on Non Uniform Rational B-Splines (NURBS). In case of strongly curved beams the simple diagonal de Saint-Venant's constitutive model can lead to significant errors as it has been reported in the classic literature. Other models like Winkler's one have been proposed and seem more suitable for these kind of structures. Unfortunately several numerical codes are based on a diagonal constitutive model which neglects the coupling effect of elongation and curvature even if a high refined geometry description can be developed by means of NURBS. The results obtained by means of numerical codes based on isogeometrical analysis for curved beams are here reported and basic choices, computational costs and numerical accuracy of the above mentioned constitutive models are discussed, from a qualitative and quantitative point of view. This comparison, in the authors' opinion, is necessary to avoid an excessive gap between the computational efficiency of NURBS, which are capable of very accurate geometry description, and a simplistic representation of the constitutive relations that is efficient for straight beams but not so much for curved beams whose curvature is large. The results of some selected tests are presented and discussed to highlight differences between the two approaches, showing that the small increase of computational cost of Winkler's model is well compensated by the accuracy gain.

1. INTRODUCTION

The last ten years were characterized by the rapid development of isogeometric approach in various fields of Mechanics. Beginning with the seminal work [1], many extensions are contained in [2] and [3] and concern a wide range of problems such as vibrations and wave propagations, nearly incompressible solids, fluids, fluid-structure interaction. Isogeometric approach generalizes some already used ideas both in finite elements, see [4, 5, 6, 7], and boundary elements [8, 9]. In these papers B-spline interpolation describes the displacements in case of finite elements and displacement and tractions in case of boundary elements.

The main advantages of the isogeometric approach, in comparison with the classical finite elements, lie basically in the application of the same tools developed for Computer Aided Design (CAD), Computer Aided Engineering (CAE) and Computer Aided Manufacturing (CAM) in the geometrical description of the mechanical problem. Hence in its capability to represent, in an exact way, conic sections such as circles and ellipses. To better understand this issue, most software packages currently used for architectural design are actually based on such CAD techniques: therefore, the ability to perform structural analyses on the same model used for design is extremely appealing. Up to now, however, researchers have concentrated their efforts more on 2D and 3D continuum models or on shell-like structures [10] than on curved beams and arches.

Only recently some papers on 1D problem have been published, even though they are particularly concerned on locking control, see [11, 12, 13, 14, 15, 16]. All these papers present the same energy form used for straight beam which is essentially derived from de Saint-Venant's theory, denoted in the following by the acronym dSV. Actually, there exist mechanical models which are especially well suited for beams with large curvature, see for example the classic paper by Winkler [17] (that will be shortened by the symbol W), which is based on simple kinematic assumptions or, more recently, those based on variational asymptotic methods to eliminate least significant terms in the elastic formulation of a 3D beam, see for instance [18, 19, 20, 21].

On the other hand, in [22, 23, 24, 25, 26] the displacements field is separated into a motion of a reference section of the beam and a 3D warping field, with both in-plane and out-of-plane components. This procedure leads, therefore, to a solution composed by a particular integral of

the differential equation (*i.e.* a polynomial solution representing the generalization of de Saint-Venant's theory which is used to compute the characteristic properties of the section) and by a general integral of the same differential equation resulting in a set of self-balanced exponential solutions which take into account boundary effects.

Already in Timoshenko's book [27] a comparison was proposed, which highlights the difference in terms of stresses resulting from assuming a strain energy corresponding to either de Saint-Venant's or Winkler's models.

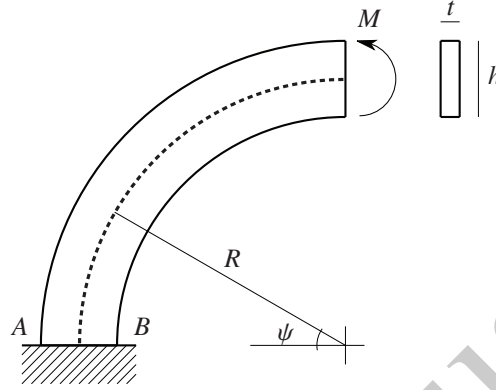


FIGURE 1. Cantilever circular arch with rectangular cross-section under pure bending load.

In order to better understand the differences between de Saint-Venant's and Winkler's models from a quantitative point of view, the 2D elastic solution of a pure bending problem is reported here: a quarter-of-circle cantilever arch with rectangular cross-section subjected to a couple acting at the free end is depicted in Figure 1. For this problem the analytical solution, assuming the hypothesis of plane stress, is known, see again [27]. In Table 1 a comparison between de Saint-Venant's, Winkler's and 2D models for the normal stress σ at both the intrados (point B) and at the extrados (point A) of the cross-section is reported. With reference to the symbols shown in Figure 1 and reinterpreting the solution provided by Timoshenko [27, pp. 71–75] the normal stress at point A can be expressed as:

$$\sigma_A = \sigma_A^* \frac{M}{t \left(R - \frac{h}{2}\right)^2}, \quad (1)$$

where σ_A^* is a suitable dimensionless coefficient. A similar expression can be used also for the stress at point B. Table 1 provides for all models above described the values of coefficients σ_A^* , σ_B^* for some selected value of the slenderness ratio h/R between section depth, h , and radius of curvature, R . The authors point out both the accuracy of Winkler's model in evaluating the stress and, on the contrary, the inaccuracy of results obtained by assuming a constitutive law based on de Saint-Venant's model. If 2D elasticity is used as a reference solution, the results provided by Saint-Venant's model produce errors ranging between 8.74% and 34.58%, while those coming out from Winkler's model lie between 0.13% and 3.1%, in a slenderness range $0.261 \leq h/R \leq 1$. Error in the displacements evaluation are instead smaller: for instance vertical deflection at the beam tip given by de Saint-Venant's model ranges between 0.55% and 7.43% when h/R varies between 0.261 and 1, see [27, pp. 75–80] for analytical results.

The goal of this work is improving the results which can be obtained by adopting numerical codes based on Non Uniform Rational B-Splines (NURBS) for curved beams. Basic choices, computational costs and numerical accuracy are discussed from a qualitative and quantitative point of view. This, in the opinion of the authors, is necessary in order to avoid an excessive gap between the computational efficiency of NURBS and a poor representation of the constitutive relations.

To achieve these goals, Section 2 introduces the problem starting from the governing differential equations for plane curved beams and, moreover, discusses different kinds of constitutive

TABLE 1. Dimensionless stress coefficient σ^* on the cross-section extrados A and intrados B with different constitutive laws: de Saint-Venant's, Winkler's and 2D elasticity.

h/R	de Saint-Venant		Winkler		2D	
	σ_A^*	σ_B^*	σ_A^*	σ_B^*	σ_A^*	σ_B^*
0.261	-66.67	66.67	-61.27	72.98	-61.35	73.05
0.667	-6.0	6.0	-4.863	7.725	-4.917	7.775
1	-1.5	1.5	-1.095	2.285	-1.130	2.293

models, highlights the main differences and similarities and looks, in particular, at the qualitative aspects. Next, in Section 3 a brief introduction of NURBS interpolation follows and the construction of a mechanical model of curved beams is shown. Then Section 4 is devoted to the presentation of the numerical results. Finally, some concluding remarks are drawn in Section 5 along with a discussion of problems, which are left opened, and future developments.

2. PROBLEM STATEMENT

Consider a plane curved beam (see Figure 2) whose centroid line is plane, curved and parametrized by the arc-length $s \in [0, \ell]$. It is also assumed that one of the principal inertia axis and the shear center of the cross-section lie in the same plane. Let the global reference system be denoted by $(O; x_1, x_2)$ and the local one by $(o; t, r)$, t and r being respectively the tangent and the normal unit vectors to the curve. Moreover, R represents the curvature radius and $(\cdot)'$ the derivatives with respect to the arc-length s . With this notation, the differential form of equilibrium and kinematic compatibility equations describing the plane curved Timoshenko beam problem in the local reference system are:

$$N' - \frac{T}{R} + q_t = 0, \quad T' + \frac{N}{R} + q_r = 0, \quad M' - T + m = 0, \quad (2)$$

$$\varepsilon = u' - \frac{w}{R}, \quad \gamma = w' + \frac{u}{R} + \varphi, \quad \chi = \varphi'. \quad (3)$$

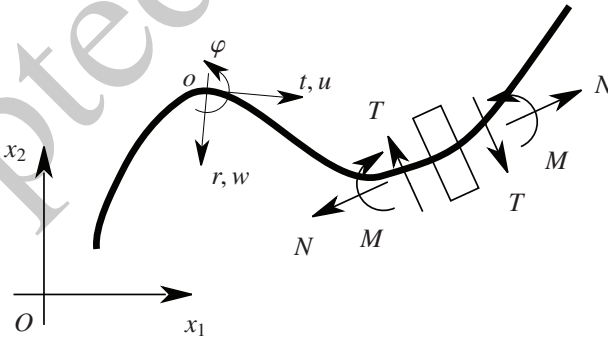


FIGURE 2. Plane curved beam: centroidal line, reference systems and positive stress components.

In Equation (2), N , T and M denote the generalized stresses (axial and shear force and bending moment, see Figure 2 for the definition of positive quantities) and q_t , q_r and m the generalized external forces per unit length (tangent and radial forces and distributed couples). In the local reference system u and w are the displacements of the axis line and φ the section rotation while ε , γ and χ denote the generalized strains (elongation, shear strain and curvature bending).

The selection of the constitutive law deserves some comments. Usually, also for curved beams, the same strain energy density is used, which has been derived from de Saint-Venant's model referred to a straight beam:

$$2\Phi = EA\varepsilon^2 + EI\chi^2 + GA_T\gamma^2, \quad (4)$$

where E and G are Young's and shear modulus, respectively, while A , I and A_T are, respectively, the cross-section area, moment of inertia and shear area.

As it has been already discussed in the Section 1, de Saint-Venant's assumptions give unsatisfactory results when strongly curved beams are considered. Winkler's model [17, 29] (see again Section 1) is essentially based on the hypothesis, which is also confirmed by experimental tests (see [27] and [28]), that the cross-section of curved beams remains plane while the stress distribution on the cross section is no more linear but follows a hyperbolic law. Thus it is considered a good compromise between simplicity and accuracy in case of stress analysis of strongly curved beams. Indeed, when the ratio h/R is small enough (say, $h/R < 0.1$) Winkler's strain energy is practically indistinguishable from de Saint-Venant's one.

Therefore, in this paper an enriched strain energy density has been implemented, whose form is:

$$2\Phi = Ec_{11}\varepsilon^2 + 2Ec_{12}\varepsilon\chi + Ec_{22}\chi^2 + Gc_{33}\gamma^2, \quad (5)$$

which encompasses both Winkler's model and that proposed by Berdichevskii and Starosel'skii in [18]. As it is simple to notice, the matrix of elastic compliance is not diagonal: there is indeed a coupling term, c_{12} , between elongation ε and bending χ .

Elastic coefficients, following Winkler's assumptions, are defined as:

$$\begin{aligned} c_{11} &= \int_A \frac{R}{R-y} dA, & c_{12} &= \int_A \frac{Ry}{R-y} dA, \\ c_{22} &= \int_A \frac{Ry^2}{R-y} dA, & c_{33} &= \int_A \frac{R^2}{b^2(R-y)^2} \left(\frac{c_{12}}{c_{22}} - \frac{\Omega}{RA} \right)^2 dA. \end{aligned} \quad (6)$$

where y is a coordinate measured along the normal r to the longitudinal axis of the beam (such direction coinciding with one of the principal inertia axis of the cross section), while Ω is the portion of the cross section area lying below the value of y . Coefficient c_{33} follows Jourawski's approximation, as it is assumed in several classic books, see for example [30]. It is important to underline (see Equation (6)) that elastic compliance coefficient c_{12} in Winkler's model depends both on cross-section geometry and on curvature radius R .

Equation (4) is often assumed as a constitutive law instead of Equation (5). In order to evaluate when this approximation is acceptable, one may consider some quantitative differences for a $t \times h$ rectangular cross-section. Figure 3 shows the differences between de Saint-Venant's and Winkler's models, as long as axial and bending behaviors are concerned, as functions of the slenderness ratio h/R . It depicts the differences d_1 and d_2 , which are defined as follows:

$$d_1 = \frac{c_{11} - A}{A}, \quad d_2 = \frac{c_{22} - I}{I}, \quad (7)$$

both of them are expressed as percentage values. Differences d_1 and d_2 highlight not negligible errors which are generally inadmissible in numerical codes. For example these errors are equal to 2% and 4% for elongation coefficient c_{11} and bending coefficient c_{22} respectively, when $h/R = 0.5$.

Equation (6) shows the elongation-bending coupling coefficient c_{12} according to Winkler's model (see Equation (6) and [17]). A different constitutive theory for strongly curved beams has been proposed by Berdichevskii's and Starosel'skii's ([18]). According to their model, strain energy density can be written in this form, too:

$$2\Phi = Ec_{11}^*\varepsilon^2 + 2Ec_{12}^*\varepsilon\chi + Ec_{22}^*\chi^2 + Gc_{33}^*\gamma^2, \quad (8)$$

where coefficients $c_{11}^* = A$, $c_{22}^* = I$ and $c_{33}^* = A_T$ coincide with those provided by de Saint-Venant's model. Instead, the Berdichevskii's and Starosel'skii's coupling coefficient c_{12}^* (see Equation (8)) depends also on Poisson's ratio ν , and is expressed in the following way:

$$c_{12}^* = \frac{(2 + \nu)I + gA}{R}, \quad (9)$$

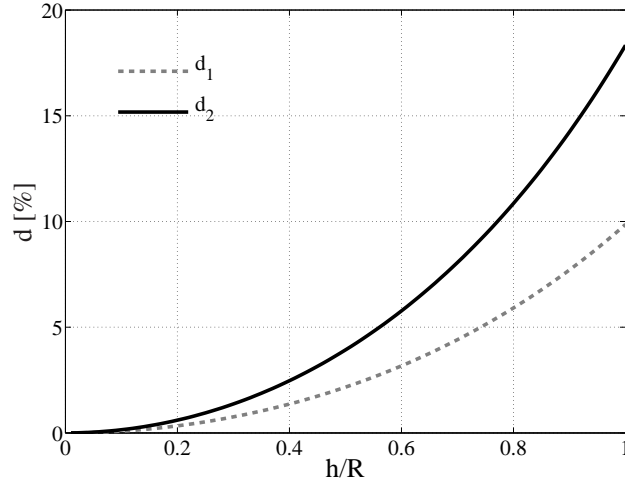


FIGURE 3. Differences, in percentage, of coefficients c_{11} , dotted line, and c_{22} , solid line, for de Saint-Venant's and Winkler's models as functions of h/R ratio.

coefficient g , appearing in Equation (9), is given by:

$$g = \frac{\nu}{15}t_2^2 + \frac{3\nu^2}{4(1+\nu)} \left(\frac{7}{15}t_2^2 + \frac{2}{9}h_2^2 + \frac{2}{45}\frac{h_2^4}{t_2^2} - \frac{4}{\pi^2}\frac{h_2^5}{t_2^3} \sum_{k=1}^{\infty} \frac{1}{k^5} \tanh \frac{k\pi t_2}{h_2} + \right. \\ \left. - \frac{128}{\pi^5}t_2h_2 \sum_{k=1}^{\infty} \frac{1}{(2k-1)^5} \coth \frac{(2k-1)\pi h_2}{2t_2} \right), \quad (10)$$

where $h_2 = h/2$ and $t_2 = t/2$ denote respectively the half-depth and the half-width of the rectangular cross section. Interestingly, the coupling coefficient is quite similar for these two models, also for higher values of h/R , especially for values of Poisson's ratio ν far from its extrema. The difference, expressed as a percentage of Winkler's c_{12} and Berdichevskii's and Starosel'skii's c_{12}^* coupling coefficients, is given by:

$$d_{12} = \frac{c_{12} - c_{12}^*}{c_{12}}, \quad (11)$$

and it is plotted in Figure 4. The maximum value is about 30% and it is reached for very small values of h/R when $\nu = 0.49$; in all other cases it is below 15%. In particular, for $\nu = 0.25$ (an average value) it turns out that the difference is steadily decreasing as the slenderness ratio h/R increases; for instance at $h/R = 1$ it is less than 2%. Consequently the influence of Poisson's ratio on the coupling effect appears to have a limited influence and this consideration allows adopting for the elongation-bending coupling coefficient the simpler form of Winkler's model instead of the more complicated Berdichevskii's and Starosel'skii's one.

Finally, in Figure 5 each term of the strain energy density, namely $Ec_{11}\varepsilon^2$ (elongation), $Ec_{22}\chi^2$ (bending), $2Ec_{12}\varepsilon\chi$ (coupled bending-elongation), $Gc_{33}\gamma^2$ (shear), for the Winkler's constitutive model, see Equation (5), is plotted versus the h/R ratio. This Figure clearly shows that the effect of the coupling coefficient c_{12} cannot be neglected, in particular for higher values of h/R , which correspond to large curvatures. The foregoing analysis strongly suggests the use of an enriched strain energy, including the elongation-bending coupling term, to improve the curved beam models. Classical Winkler's model, in the authors' opinion, is a smart choice since it combines simplicity and effectiveness besides providing results in agreement with independently generated variational asymptotic methods deduced from 3D elasticity like the Berdichevskii's and Starosel'skii's model.

3. ISOGEOMETRIC DISCRETIZATION

In this paper the geometry of a curved beam is described by means of a NURBS interpolation; for a complete and more accurate description of this kind of interpolation please see [31]. It can be stated that a curve $\mathbf{x} = \mathbf{x}(\xi)$ has a p -degree NURBS representation when there exist $n \in \mathbb{N}$,

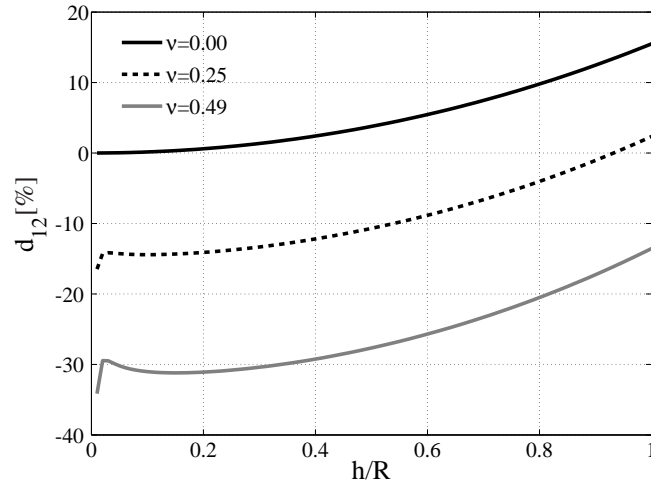


FIGURE 4. Percentage difference between Winkler's and Berdichevskii's and Starosel'skii's coupling coefficients for different values of Poisson's ratio.

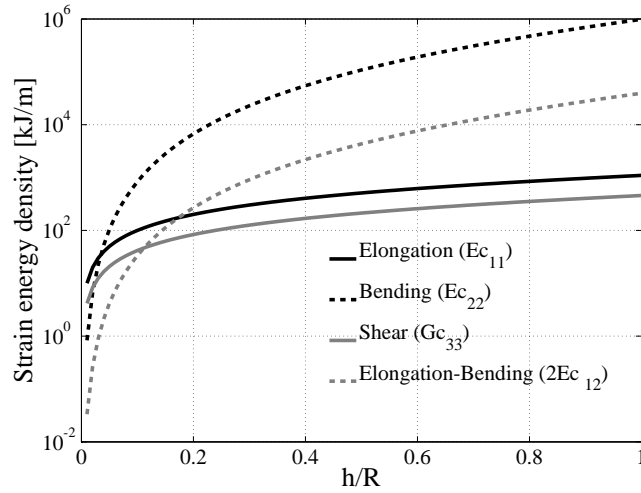


FIGURE 5. Strain energy density contributions for Winkler's model referred to a circular arch (with $h \times t$ rectangular cross-section) as a function of slenderness ratio h/R . Unit values are assumed for generalized strain components ε , γ and χ . Geometric and mechanical properties: $R = 1$ m; $t = 10$ mm; $10 \leq h \leq 1000$ mm; $E = 10$ MPa; $G = 5$ MPa.

control points $\mathbf{P}_i \in \mathbb{R}^2$, with the associated weights $g_i \in \mathbb{R}$, $i = 1 \dots n$, and a *knot vector*, i.e. a set $\Xi = \{0 = \xi_1 \leq \xi_2 \leq \dots \leq \xi_{n+p+1} = 1\}$ such that, for any $\xi \in [0, 1]$:

$$\mathbf{x}(\xi) = \sum_{i=1}^n R_{i,p}(\xi) \mathbf{P}_i, \quad (12)$$

where the NURBS basis $\{R_{i,p}(\xi)\}$ is expressed by:

$$R_{i,p}(\xi) = \frac{B_{i,p}(\xi)g_i}{\sum_{i=1}^n B_{i,p}(\xi)g_i}. \quad (13)$$

The Cox-De Boor recursive formula defines the B-splines basis $\{B_{i,p}(\xi)\}$ of order p as a function of the basis corresponding to order $p - 1$:

$$B_{i,0}(\xi) = \begin{cases} 1 & \text{if } \xi_i \leq \xi < \xi_{i+1} \\ 0 & \text{otherwise} \end{cases}, \quad (14)$$

$$B_{i,p}(\xi) = \frac{\xi - \xi_i}{\xi_{i+p} - \xi_i} B_{i,p-1}(\xi) + \frac{\xi_{i+p+1} - \xi}{\xi_{i+p+1} - \xi_{i+1}} B_{i+1,p-1}(\xi). \quad (15)$$

The so-called knot vector Ξ is a non-decreasing set of coordinates which defines a partition of the parameter space $[0, 1]$. The knots divide the parameter space into elements similarly to what happens into the classical finite element discretization, see Figure 6. NURBS allow to develop a very refined geometric description; *non-uniform knot vectors* and *repeated knots* are the key ingredients of their flexibility and efficiency.

A *non uniform knot-vector* corresponds to a set of unequally spaced knots, which allow representing a larger number of shapes. The *multiplicities* of *knot values* have important effects on the properties of the basis. Actually a basis function of order p has $p - m_i$ continuous derivatives at knot ξ_i where m_i is the multiplicity of value ξ_i in the knot vector. A natural consequence of the latter statement is the high-degree of continuity of NURBS, which is one of their most interesting properties. In particular, each p -th order function is of class C^{p-1} , *i.e.* it is continuous with its derivatives up to $(p - 1)$ -th order, and it is smooth across the boundaries. The continuity degree can be reduced, if needed, by using repeated knots, see Figure 7. Furthermore, the introduction of weights g_i related to i -th control point improve the capabilities of the B-splines interpolation allowing also for an exact representation of circles, ellipses and other curves obtained by conic sections.

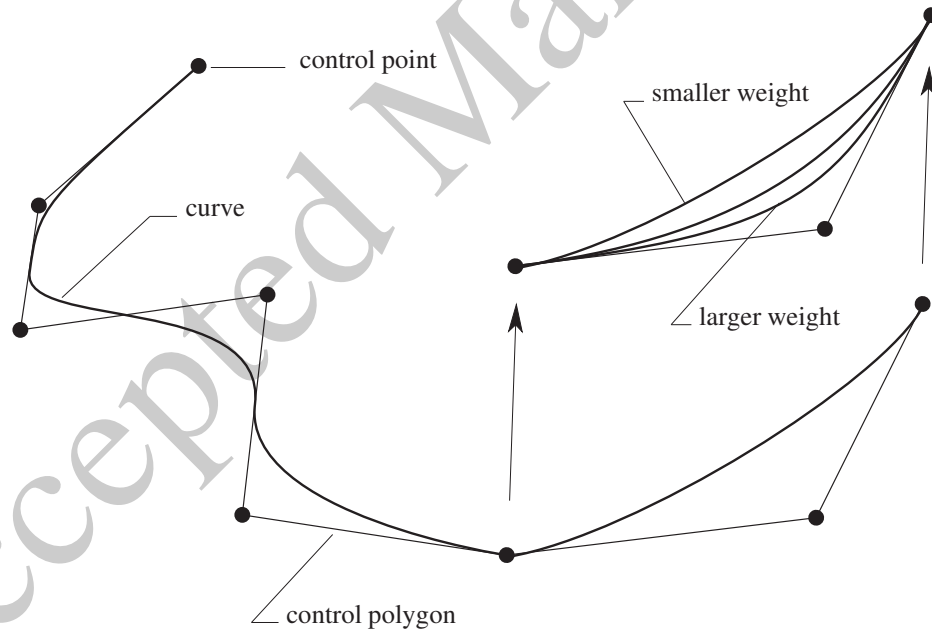


FIGURE 6. NURBS basic ingredients: control points (\bullet), control polygon, curve and influence of the control point weights.

The main goal of the isogeometric approach is to exactly describe the geometry of the problem by means of NURBS interpolation and to adopt the same interpolating basis for representing the generalized displacements:

$$u(\xi) \approx \sum_{i=1}^n R_{i,p}(\xi) u_i, \quad w(\xi) \approx \sum_{i=1}^n R_{i,p}(\xi) w_i, \quad \varphi(\xi) \approx \sum_{i=1}^n R_{i,p}(\xi) \varphi_i, \quad (16)$$

by means of control points u_i , w_i , and φ_i .

If a dot is used to represent the derivatives of any function with respect to ξ and J denotes the Jacobian of the transformation, from basic differential geometry (see [32]) it follows:

$$J = \dot{s} = \sqrt{\dot{x}_1^2 + \dot{x}_2^2}, \quad R = \frac{J^3}{|\dot{x}_1 \ddot{x}_2 - \ddot{x}_1 \dot{x}_2|}. \quad (17)$$

Hence, the generalized strains assume this form:

$$\varepsilon = \frac{\dot{u}}{J} - \frac{w}{R}, \quad \gamma = \frac{\dot{w}}{J} + \frac{u}{R} + \varphi, \quad \chi = \frac{\dot{\varphi}}{J}. \quad (18)$$

Referring to the elastic strain energy density Φ defined by Equation (4) or by Equation (5), see Section 2, the discretized form of total potential energy can be written as:

$$\arg \min_{u,w,\varphi} \left\{ \sum_{e=1}^{n_e} \left(\frac{1}{2} \int_{\xi_e}^{\xi_{e+1}} \Phi J d\xi - \int_{\xi_e}^{\xi_{e+1}} (q_t u + q_r w + m\varphi) J d\xi \right) \right\}, \quad (19)$$

where n_e is the number of subdivision of the parameter space. Enforcing Equation (19) produces a linear system of equations where the unknowns are values of the control points u_i , w_i and φ_i . The integrals which are necessary to obtain the stiffness matrix and the load vector are evaluated numerically by using Gauss's quadrature rule, even if integrand functions are not generally polynomials. Reference [3] provides some guidelines about the choice of the number of Gauss points for an efficient quadrature rule. In this paper the number of points is always assumed equal to the degree p of the spline basis functions due to its efficiency as proved in [33]. Furthermore, this also helps in preventing locking problems such as those described in [13].

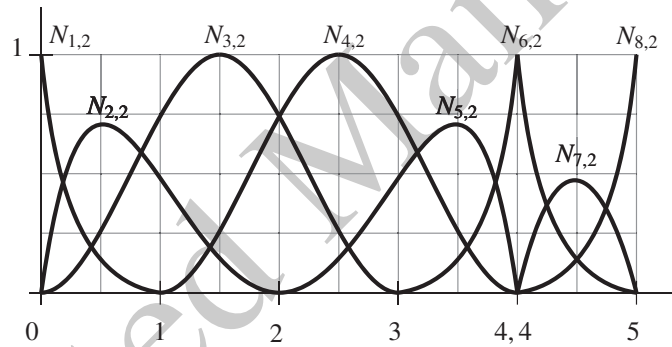


FIGURE 7. Effect of repeated knots on NURBS construction: in 2nd-order NURBS the repeated 5th knot reduces the continuity degree of the curve at that point (knot indexes are shown on the horizontal axis and the knot vector is $\Xi = \{0, 0, 0, 1, 2, 3, 4, 4, 4, 5, 5, 5\}$).

4. NUMERICAL RESULTS

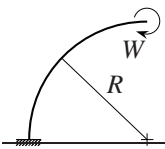
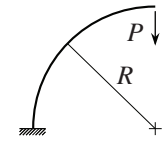
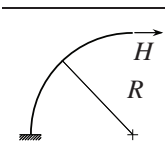
In this section the differences between Winkler's and de Saint-Venant's constitutive models are explored and discussed by means of analytical computations and by a numerical code based on IGA (*i.e.* IsoGeometric Analysis). For plane curved beams exhibiting strong curvature under different load conditions several test cases are presented.

4.1. Cantilever circular arch. The results concerning a cantilever circular arch are presented in this subsection. In Table 2 the theoretical results for both classical de Saint-Venant's and Winkler's models are shown; the arch is clamped at one end, different loading conditions are applied at free end. These are denoted simply by LC1 (bending couple, W), LC2 (vertical force, P), LC3 (horizontal force, H) see Table 2. The used load values are respectively: $W = 10$ kNm, $P = 10$ kN, $H = 10$ kN. The results are computed for an arch whose radius of curvature is $R = 1$ m, having a rectangular cross section with constant width $t = 0.2$ m and variable depth h such that $1/100 \leq h/R \leq 4/5$ in order to explore the influence of the slenderness ratio. Elastic mechanical parameters are: Young's modulus $E=1$ GPa, Poisson's ratio $\nu=0.2$, which provide $G = 0.4167$

GPa. The closed-form analytical solutions, which are used for comparison, are taken from [33] and from the Appendix of this paper.

It is clear from Table 2 that the difference between de Saint-Venant’s and Winkler’s models is increasing when also the h/R ratio increases; on the contrary it becomes very small when h/R tends to zero.

TABLE 2. Dimensionless values of tip deflection, f , and maximum σ^+ and minimum σ^- normal stress at clamped end for a cantilever circular arch. Closed-form solutions for Winkler’s model (W) are scaled by the corresponding de Saint-Venant’s analytic solutions (dSV).

Load case	h/R	f_W/f_{dsv}	$\sigma^-_W/\sigma^-_{dsv}$	$\sigma^+_W/\sigma^+_{dsv}$
	1/100	0.99998	1.00333	0.99667
	1/10	0.99850	1.03440	0.96763
	1/5	0.99399	1.07110	0.93696
	2/3	0.93240	1.28754	0.81043
	4/5	0.90204	1.37013	0.77769
	1/100	0.99998	0.98852	0.99666
	1/10	0.99767	1.03384	0.96708
	1/5	0.99426	1.06881	0.93479
	2/3	1.04700	1.25879	0.78673
	4/5	1.05623	1.32659	0.74348
	1/100	1.00010	1.00333	0.99667
	1/10	1.01102	1.00333	0.99667
	1/5	1.00085	1.07110	0.93696
	2/3	1.11948	1.28754	0.81043
	4/5	1.22231	1.37013	0.77769

The difference between de Saint-Venant’s and Winkler’s approaches is clearly shown in Figure 8, where the stress distribution along the section depth is shown for $h/R = 2/3$ and for a generic bending or shear load case.

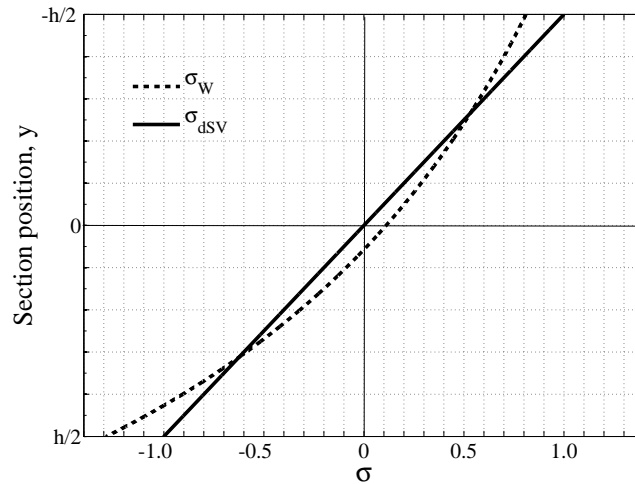
The numerical code has been tested considering closed-form solution presented in the Appendix of this paper. Assuming $h/R = 2/3$, Figure 9 presents percentage error e of the deflection f :

$$e = \left\| 1 - \frac{f_{num}}{f} \right\|, \tag{20}$$

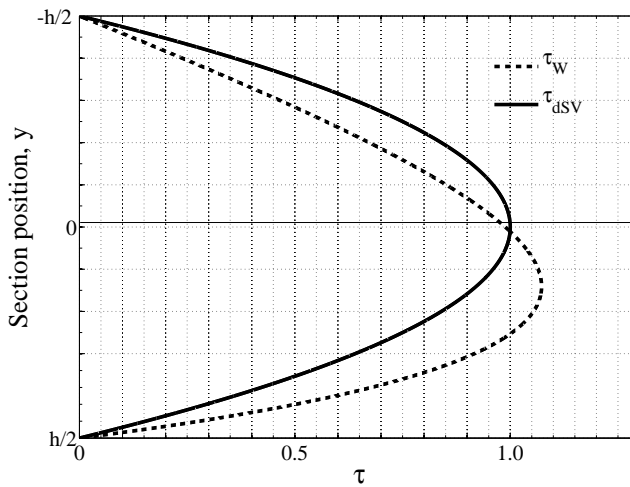
for various NURBS order p and element number n_e . A Winkler’s model of the above mentioned cantilever circular arch is considered under the three already defined loading conditions. It is clear that convergence is achieved even with a low-order NURBS interpolation and with a small number of elements.

Similar comparisons between the theoretical values and the numerical ones are obtained considering the stress at the clamped end of the circular arch: the ratios between the numerical and the analytical values of the maximum and minimum stresses are presented in Table 3. In all cases the code appears to be very efficient producing excellent results also with low order NURBS and small element numbers.

In addition no significant computational time increase has been detected for Winkler’s model. This is shown in Table 4 where the computational time for de Saint-Venant’s (left) and Winkler’s (right) implementation is shown for the same circular arch and the same load conditions. The numerical code, developed in MATLAB environment (*R.2013.a*) has been tested on a 64-bit machine characterized by 8 GB of RAM memory, 2.6 GHz Intel Core i5 CPU. In order to minimize the effect of the intrinsic CPU clock time error, ten runs have been performed for each case and then their average has been computed and reported in Table 4. For the sake of synthesis only a cantilever circular arch characterized with $h/R = 2/3$ (*i.e.* a rather large value, where the difference between the two models is expected to be large) has been considered. Looking at Table 4, Winkler’s model is slower at most by an amount of 10^{-3} s in comparison with de Saint-Venant’s



(a) Normal stress distribution



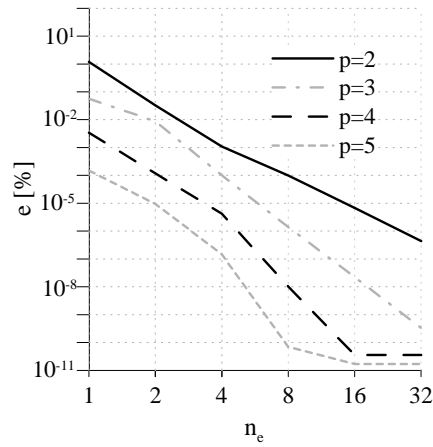
(b) Shear stress distribution

FIGURE 8. Comparison for slenderness ratio $h/R = 2/3$ between de Saint-Venant's (dSV) and Winkler's (W) models in terms of normal (a) and shear (b) stress distributions. Cross section is rectangular with depth h , under shear and bending load. Plotted distribution are scaled by the maximum values of de Saint-Venant's solution.

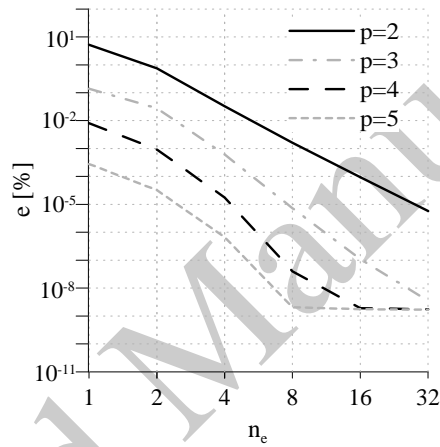
model. This can be somehow justified by the shape of the stiffness matrix which produces more coupling in equations in the former case than in the latter.

4.2. Circular chain ring. Table 5 presents the maximum and minimum normal stress at two significant section, A and B , of a circular chain ring under two equal and opposite compressive forces whose value is $P = 1$ kN. The arch cross section is rectangular as it is shown in Figure 10. The same Figure represents the location of sections A and B , the structure geometry along with the simplified structural model, account taken of symmetry. The width of the cross section $t = 0.2$ m, its depth is $h/R = 2/3$ while the curvature radius R is equal to 1 m; the elastic Young's modulus is $E=1$ GPa, and the Poisson's ratio is $\nu = 0.2$.

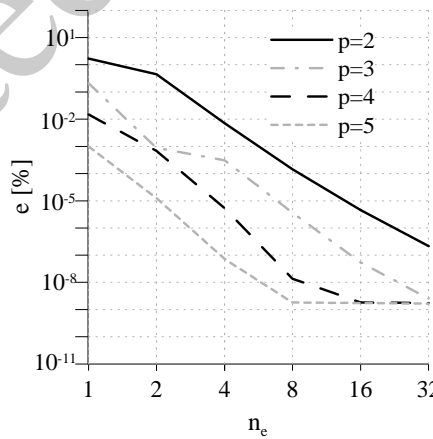
A reference solution is reported by Belluzzi in [34] and despite his considering both de Saint-Venant's and Winkler's models it was obtained neglecting the shear strain. This approximation



(a) bending couple, $W = 10$ kNm



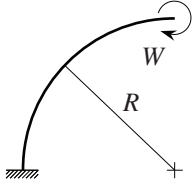
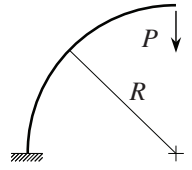
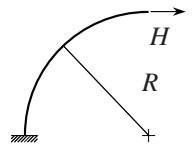
(b) vertical force $P = 10$ kN



(c) horizontal force $H = 10$ kN

FIGURE 9. Cantilever circular arch with $h/R = 2/3$ by Winkler's model; tip deflection error for different load conditions.

TABLE 3. Cantilever circular arch with $h/R = 2/3$ by Winkler's model; minimum σ_- and maximum σ_+ normal stress are computed at clamped end. Reported numerical values are scaled by the theoretical ones.

Load case	p	n_e							
		1	2	4	8	16	32		
	σ_+	2	1.4852	1.1113	1.0251	1.0061	1.0015	1.0004	
		3	1.0238	1.0093	1.0008	1.0001	1.0000	1.0000	
		4	1.0077	1.0008	1.0001	1.0000	1.0000	1.0000	
		5	1.0000	1.0002	1.0000	1.0000	1.0000	1.0000	
	σ_-	2	0.2598	0.8339	0.9613	0.9905	0.9976	0.9994	
		3	0.9860	0.9881	0.9986	0.9998	1.0000	1.0000	
		4	0.9863	0.9986	0.9999	1.0000	1.0000	1.0000	
		5	0.9988	0.9996	1.0000	1.0000	1.0000	1.0000	
		σ_+	2	1.4002	1.1945	1.0443	1.0105	1.0026	1.0006
			3	1.0934	0.9987	0.9982	0.9998	1.0000	1.0000
		4	0.9855	0.9943	1.0002	1.0000	1.0000	1.0000	
		5	0.9950	1.0004	1.0000	1.0000	1.0000	1.0000	
σ_-		2	0.4259	0.8190	0.9592	0.9899	0.9975	0.9994	
		3	0.9730	1.0108	1.0016	1.0002	1.0000	1.0000	
		4	1.0282	1.0053	0.9998	1.0000	1.0000	1.0000	
		5	1.0000	0.9994	1.0000	1.0000	1.0000	1.0000	
		σ_+	2	0.8487	1.0194	1.0200	1.0055	1.0014	1.0004
			3	1.0683	1.0264	1.0010	1.0001	1.0000	1.0000
		4	1.0168	1.0022	1.0000	1.0000	1.0000	1.0000	
		5	1.0026	1.0002	1.0001	1.0000	1.0000	1.0000	
	σ_-	2	0.5949	0.8519	0.9637	0.9908	0.9977	0.9994	
		3	0.9302	0.9899	1.0000	1.0000	1.0000	1.0000	
		4	1.0087	0.9967	0.9998	1.0000	1.0000	1.0000	
		5	0.9954	0.9987	0.9999	1.0000	1.0000	1.0000	

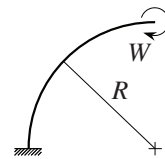
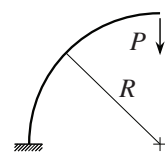
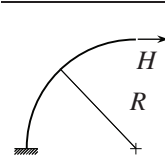
can explain the very small differences with respect to the numerical solution: by taking a NURBS order $p = 5$ and an eight-element mesh the maximum error is lower than 0.5% while the minimum is 0.07%. Furthermore a closed-form solution has been obtained integrating the governing equations: see Appendix. Both de Saint-Venant's and Winkler's models have been considered, the results present negligible differences in comparison with the numerical solution.

4.3. Elliptical chain ring. The radial displacements at sections A, B (see Figure 11) of an elliptical chain ring, characterized by semi-major axis $a = 2D$, semi-minor axis $b = 3D/2$ are reported in Table 6. The cross-section is circular with a diameter $D = 0.1$ m; two equal and symmetrically placed tensile forces $P = 10$ kN are applied at both ends of the major axis. As usual the elastic parameters are: $E=1$ GPa, $\nu = 0.2$. Again, because of symmetry only a quarter of ellipse is considered for computation (see Figure 11).

The analytical solution has been obtained integrating the governing equations. Both de Saint-Venant's and Winkler's constitutive models have been considered (see Appendix for the analytical expressions). However in the latter case, it was necessary to introduce an approximation assuming that stiffness coefficients do not change with curvature radius.

Indeed, if the complete form of Equation (6) is taken, the resulting governing equations cannot be integrating exactly and no closed-form solution can be reached. The proposed solution for the Winkler's model is therefore an approximated one; on the other hand a two-fold consideration applies. First, since the variation of curvature radius within the structure is not so large ($0.1125 \leq R \leq 0.2667$ m) and moreover the slenderness ratio varies in a limited range ($3/8 \leq D/R \leq 8/9$), it is expected that the variation of stiffness coefficients is suitably limited, and the error introduced by assuming them to be constant is also suitably limited. Thus, by looking at the minima and maxima of the stiffness coefficients it is always possible to define a suitable range bracketing

TABLE 4. Cantilever circular arch: CPU time [s] spent by the codes implementing both de Saint-Venant's and Winkler's models as functions of NURBS order, p , and number of elements, n_e .

	n_e	de Saint-Venant				Winkler			
		p				p			
		2	3	4	5	2	3	4	5
	1	0.169	0.171	0.170	0.170	0.171	0.171	0.171	0.171
	2	0.175	0.175	0.177	0.177	0.176	0.177	0.179	0.178
	4	0.179	0.179	0.181	0.178	0.180	0.180	0.182	0.181
	8	0.180	0.182	0.183	0.182	0.180	0.181	0.181	0.185
	16	0.184	0.184	0.187	0.187	0.183	0.185	0.187	0.190
	32	0.188	0.192	0.196	0.200	0.188	0.194	0.196	0.202
	1	0.169	0.171	0.170	0.171	0.171	0.171	0.171	0.173
	2	0.176	0.176	0.177	0.178	0.178	0.179	0.179	0.180
	4	0.176	0.178	0.177	0.180	0.179	0.180	0.180	0.180
	8	0.178	0.179	0.181	0.182	0.183	0.184	0.184	0.184
	16	0.182	0.183	0.185	0.192	0.183	0.185	0.188	0.191
	32	0.186	0.189	0.194	0.202	0.189	0.192	0.197	0.201
	1	0.170	0.171	0.171	0.171	0.174	0.174	0.174	0.174
	2	0.176	0.176	0.177	0.177	0.179	0.179	0.179	0.179
	4	0.177	0.178	0.180	0.180	0.179	0.180	0.181	0.180
	8	0.179	0.179	0.181	0.184	0.180	0.182	0.184	0.182
	16	0.181	0.183	0.186	0.190	0.183	0.186	0.188	0.193
	32	0.187	0.191	0.196	0.200	0.188	0.192	0.197	0.203

on both sides, above and below, the actual solution. Finally a possible strategy for approaching, with an arbitrary precision, the real solution can be devised in this way: one can assume that stiffness coefficients are constant only on each subdomains which the arch can be divided into. The solution for each subdomain is easily computed and the complete solution can be obtained by properly matching these partial solutions by enforcing stress and displacement continuity at each subdomain boundary. In Table 6 the reference solutions for de Saint-Venant's model, where the stiffness coefficients are really constant, are exact and match perfectly the numerical ones. Instead for the Winkler's model, the approach outlined above has been implemented, and the maxima and minima of the stiffness coefficients were evaluated and the corresponding solutions defined a range encompassing the real solution. Looking at Table 6 it is apparent that the numerical solution perfectly fits this range and this proves the accuracy of the code.

4.4. Cantilever Elliptical Arch. Tables 7-12 show the numerical results for both the classical de Saint-Venant's and Winkler's approaches for the case of a cantilever elliptical arch. It is clamped at one end and two different loading conditions are applied at the free end. These are denoted as already presented in the case of cantilever circular arch by LC1 (bending couple, $W=10$ kNm) and by LC3 (horizontal force, $H=10$ kN). Arch geometry data are the following: $b=1$ m (semi-minor axis) $a=1.5$ m (semi-major axis), rectangular cross section with constant width $t=0.2$ m and depth h varying in the range $b/10 \leq h \leq 2b/3$, in order to explore the influence of the slenderness h/b . Elastic parameters are: $E=1$ GPa, $\nu=0.2$. As it has been previously proved (see Table 2), the difference between de Saint-Venant's and Winkler's models increase with the h/b ratio, while when it is very small there is, practically no difference between the two models.

Radial (vertical) tip deflections (\hat{w}) are calculated and reported in Tables 7, 9, 11; the corresponding tangential (horizontal) tip displacements (\hat{u}) are instead shown in Tables 8, 10, 12. Reported values are written in dimensionless form; the corresponding actual values w and u can be deduced by the following equations:

$$\hat{w} = 1000 \frac{w}{t} \left(\frac{h}{b} \right)^3, \quad \hat{u} = 1000 \frac{u}{t} \left(\frac{h}{b} \right)^3. \quad (21)$$

TABLE 5. Circular chain ring with rectangular cross section, $h/R = 2/3$: normal stress [kPa] at sections A and B , see Figure 10. Load value is $P = 1$ kN. Both de Saint-Venant's and Winkler's models are considered as functions of number of elements, n_e , and NURBS order, p .

	p	de Saint-Venant			Winkler		
		n_e			n_e		
		2	4	8	2	4	8
σ_A	2	19.985	21.750	21.576	25.637	27.099	26.747
	3	22.364	21.521	21.490	27.840	26.653	26.612
	4	21.607	21.487	21.486	26.582	26.596	26.607
	5	21.506	2.1489	21.486	26.561	26.611	26.607
	Analytic [34]		21.486 21.450			26.607 26.625	
$\sigma_{A'}$	2	-17.212	-20.542	-21.257	-13.741	-16.150	-16.596
	3	-20.973	-21.472	-21.484	-16.526	-16.742	-16.747
	4	-21.455	-21.479	-21.486	-16.844	-16.747	-16.748
	5	-21.453	-21.484	-21.486	-16.758	-16.747	-16.748
	Analytic [34]		-21.486 -21.450			-16.748 -16.725	
σ_B	2	-19.672	-16.869	-16.210	-26.266	-21.719	-20.846
	3	-16.226	-15.973	-16.011	-20.958	-20.539	-20.593
	4	-15.840	-16.020	-16.014	-20.351	-20.606	-20.598
	5	-16.019	-16.015	-16.014	-20.600	-20.599	-20.597
	Analytic [34]		-16.014 -15.975			-20.597 -20.625	
$\sigma_{B'}$	2	6.814	8.196	8.437	6.402	6.743	6.820
	3	8.559	8.527	8.515	6.971	6.858	6.855
	4	8.636	8.510	8.514	6.919	6.853	6.854
	5	8.502	8.514	8.514	6.844	6.855	6.855
	Analytic [34]		8.514 8.475			6.855 6.825	

TABLE 6. Elliptical chain ring with circular cross section (diameter $D = 0.1$ m), see Figure 11, $a = 2D$, $b = 3D/2$): radial tip deflection [mm] w_A and w_B under the effect of two equal and opposite forces $P = 10$ kN. Comparison between de Saint-Venant's and Winkler's solutions as functions of number of elements, n_e , and NURBS order, p .

	p	de Saint-Venant				Winkler			
		n_e				n_e			
		4	8	16	32	4	8	16	32
w_A	2	-0.5762	-0.5782	-0.5783	-0.5783	-0.8345	-0.8363	-0.8364	-0.8364
	3	-0.5783	-0.5783	-0.5783	-0.5783	-0.8362	-0.8364	-0.8364	-0.8364
	4	-0.5783	-0.5783	-0.5783	-0.5783	-0.8364	-0.8364	-0.8364	-0.8364
	5	-0.5783	-0.5783	-0.5783	-0.5783	-0.8364	-0.8364	-0.8364	-0.8364
	Analytic		-0.5783				-0.8701 ... -0.8041		
w_B	2	0.4516	0.4531	0.4532	0.4532	0.7654	0.7664	0.7664	0.7664
	3	0.4531	0.4532	0.4532	0.4532	0.7664	0.7664	0.7664	0.7664
	4	0.4532	0.4532	0.4532	0.4532	0.7664	0.7664	0.7664	0.7664
	5	0.4532	0.4532	0.4532	0.4532	0.7664	0.7664	0.7664	0.7664
	Analytic		0.4532				0.7298 ... 0.8044		

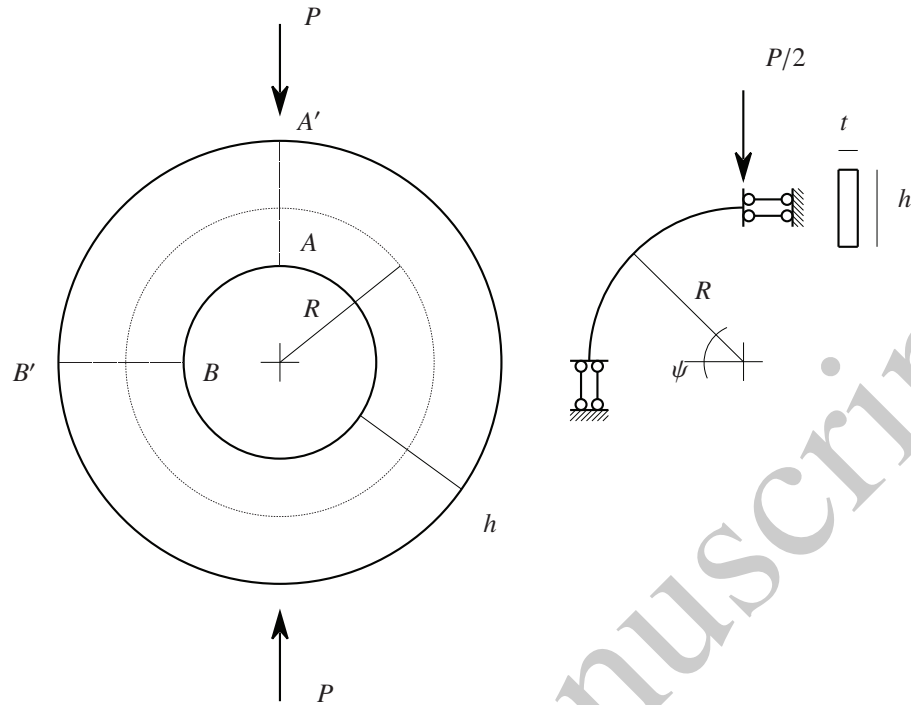


FIGURE 10. Circular chain ring with rectangular cross section: geometry and adopted structural scheme. Points A' and B' lie on the outer boundary (extrados), while the corresponding points A and B are located on the inner one (intrados).

For de Saint-Venant's model, the analytical solution has been computed by integrating the governing equations as it has been proposed in [35] and [36]; the correct solution is reported in the Appendix. The numerical solution perfectly matches the closed-form one in this case, too.

For Winkler's model, the authors have provided again an approximate analytical solution. As it was said before in Section 4.3, this solution is based on the assumption that stiffness coefficients are constant. Then, in the post processing phase their maxima and minima were evaluated and the corresponding range, bracketing the real solution, have been identified. The numerical solution perfectly fits, also in this case, the above mentioned range ensuring the accuracy which can be achieved by the code.

Actually in Table 7 and 8 (corresponding to $h/b=1/10$) the differences between de Saint-Venant's and Winkler's numerical results are practically negligible. These differences increase to 0.5% in Table 9 and 10 (corresponding to $h/b=1/5$) and become quite significant in Table 11 and 12 (corresponding to $h/b=2/3$).

The numerical code proved to be consistent and efficient: the convergence is reached with 4...8 elements for NURBS order $p = 3...4$ or even with less elements for higher values of p . In particular the error of the numerical solution is negligible, in both the loading cases considered here, for $n_e > 2$ and $p > 2$.

The computational time of the code implementing de Saint-Venant's approach (left) and Winkler's one (right) are reported in Table 13. The numerical code, developed in MATLAB environment (*R.2013.a*) has been tested on a 64-bit machine characterized by 8 GB of RAM memory, 2.6 GHz Intel Core i5 CPU. As it was done before, in order to reduce the influence of the intrinsic CPU clock time error ten runs for each case have been performed and their average values are reported. For the sake of synthesis, only an arch characterized by high curvature $h = b/5$ (on of the more interesting in terms of differences of computational cost) has been considered. Looking at Table 13 one can note that Winkler's model is slower by an amount of few milliseconds in comparison with de Saint-Venant model; indeed in the former case the shape of the stiffness matrix

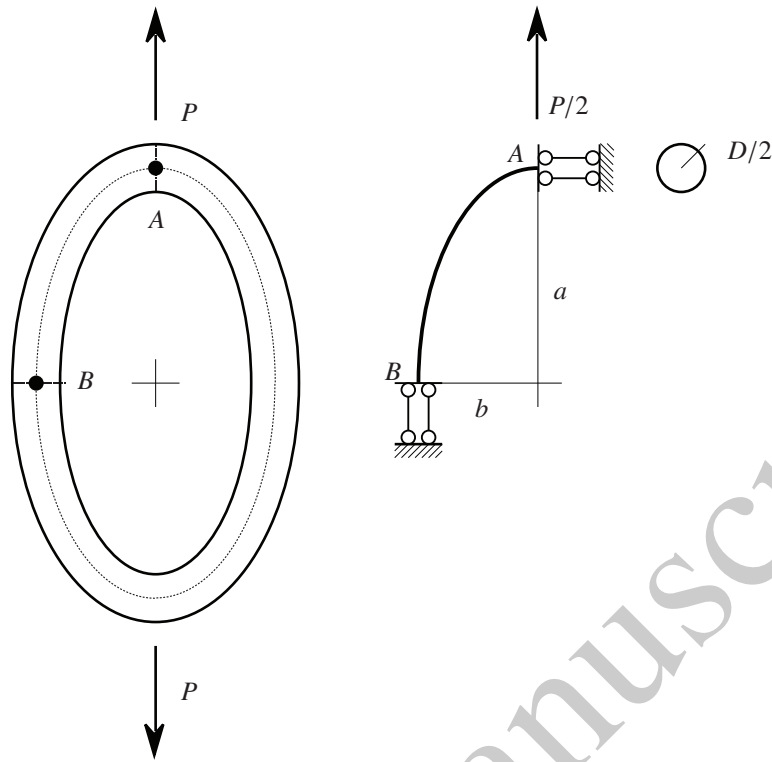


FIGURE 11. Elliptical chain ring with circular cross section: geometry and adopted structural scheme. Points A and B lie on the centroidal line.

produces equations which are more coupled than in the latter case, thus requiring a longer CPU time.

5. CONCLUDING REMARKS

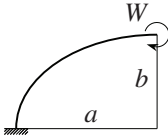
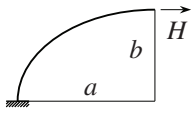
This work presented the results obtained by means of NURBS-based numerical codes for curved beams and discussed, from a qualitative and quantitative point of view, basic choices, computational costs and numerical accuracy of two well known constitutive models. The former is due to de Saint-Venant and assumes a diagonal constitutive matrix where elongation is related to axial force only and, similarly, curvature is linked to bending moment only. The latter is Winkler's model, which is well suited for beams with large curvature, and is based on simple kinematic assumptions which lead to a coupling of axial and bending behaviors.

This comparison, in the authors' opinion, shows that the computational efficiency of NURBS, which provide a very accurate geometric description, should not be jeopardized by the use of a simplistic representation of the constitutive relations. These are correct for straight beams and still acceptable for slightly curved ones but not for strongly curved members, where the occurrence of a non linear initial shape must be explicitly accounted for. Indeed, the numerical results presented in Section 4 highlight that the differences between de Saint-Venant's and Winkler's models are important only when the curvature become significant (namely, $h/R > 1/5$, as it has been already shown).

The adoption of Winkler's constitutive model instead of de Saint-Venant's one requires a slight increase (approximately 5...7%) of the computational cost but produces a much higher increase of accuracy (up to 30% when stress evaluation is concerned as it has been shown in Table 1) in the case of strongly curved beams. As a consequence for an accurate isogeometric analysis of plane curved beams with $h/R > 1/5$ Winkler's constitutive model must be adopted.

Possible future developments of this research can be outlined as follows:

TABLE 7. Dimensionless radial tip deflection \hat{w} of a cantilever elliptical arch with $h \times t$ rectangular cross section and slenderness ratio $h/b = 1/10$ under bending couple $W = 1$ kNm or horizontal force $H = 1$ kN. Comparison between de Saint-Venant’s (dSV) and Winkler’s (W) solutions as functions of number of elements, n_e , and NURBS order, p . Actual radial tip deflection w is related to the given one by Equation (21).

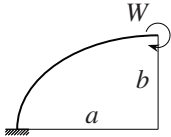
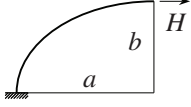
		p	n_e					
			2	4	8	16	32	64
	dSV	2	0.2856	0.4966	0.5289	0.5310	0.5312	0.5312
		3	0.5149	0.5307	0.5312	0.5312	0.5312	0.5312
		4	0.5302	0.5311	0.5312	0.5312	0.5312	0.5312
		5	0.5311	0.5312	0.5312	0.5312	0.5312	0.5312
		Analytic	0.5312					
	W	2	0.4849	0.5284	0.5305	0.5306	0.5306	0.5306
		3	0.5166	0.5302	0.5306	0.5306	0.5306	0.5306
		4	0.5294	0.5305	0.5306	0.5306	0.5306	0.5306
		5	0.5305	0.5306	0.5306	0.5306	0.5306	0.5306
		Analytic	0.5296...0.5312					
	dSV	2	0.1517	0.2325	0.2456	0.2464	0.2465	0.2465
		3	0.2364	0.2462	0.2465	0.2465	0.2465	0.2465
		4	0.2453	0.2464	0.2465	0.2465	0.2465	0.2465
		5	0.2464	0.2465	0.2465	0.2465	0.2465	0.2465
		Analytic	0.2465					
	W	2	0.2415	0.2452	0.2463	0.2463	0.2463	0.2463
		3	0.2386	0.2461	0.2463	0.2463	0.2463	0.2463
		4	0.2450	0.2462	0.2463	0.2463	0.2463	0.2463
		5	0.2463	0.2463	0.2463	0.2463	0.2463	0.2463
		Analytic	0.2460...0.2468					

- static analysis of more complicated shapes (lancet arch etc), like those presented in [37] for historic masonry arches, where only de Saint-Venant’s model has been considered until now;
- buckling problems following the way traced into [38, 39, 40, 41] and the papers cited therein;
- dynamic analysis of curved beams in the framework of isogeometric analysis, as an extension of the works [42] and [11];
- extension to mixed-hybrid methods [43, 44, 45] which provide more accurate stress description also in the case of layered structures [46];
- mathematical model improvement, for example using a suitable damage parameter [47, 48, 49] taking into account that in some cases it leads to non-unique and non-stable solutions, see [50, 51, 52]. Alternatively, there is the way proposed in [53, 54], where a two-dimensional model for an interfacial zone is introduced and this could be used to describe concentrated damages. Furthermore, the variational techniques presented in [55], being adapted to dissipative phenomena, may be of used in this context. Finally, it seems attractive the application of higher continuum models as those described in [56, 57, 58, 59];
- damage detection referring to the procedure proposed by [60, 61] which considers traveling loads as signal or in identification problem such as those described in [62, 63, 64, 65];
- the extension to plasticity for evaluating collapse load, see for example [66, 67, 68, 69, 70, 71].

APPENDIX A. SOME CLOSED-FORM SOLUTIONS

A.1. **Cantilever circular arch: de Saint-Venant’s model.** The closed-form solution for load cases LC1 (bending couple, W) and LC2 (vertical force, P) are given in [33]. For the last case

TABLE 8. Dimensionless tangential tip displacement \hat{u} of a cantilever elliptical arch with $h \times t$ rectangular cross section and slenderness ratio $h/b = 1/10$ under bending couple $W = 1$ kNm or horizontal force $H = 1$ kN. Comparison between de Saint-Venant's (dSV) and Winkler's (W) solutions as functions of number of elements, n_e and NURBS order, p . Actual (dimensional) tangential tip deflection u is related to the given one by Equation (21)₂.

		n_e						
		p	2	4	8	16	32	64
	dSV	2	0.1167	0.1813	0.1904	0.1910	0.1911	0.1911
		3	0.1826	0.1909	0.1911	0.1911	0.1911	0.1911
		4	0.1904	0.1910	0.1911	0.1911	0.1911	0.1911
		5	0.1910	0.1911	0.1911	0.1911	0.1911	0.1911
	Analytic	0.1911						
	W	2	0.1857	0.1905	0.1911	0.1911	0.1911	0.1911
		3	0.1838	0.1910	0.1911	0.1911	0.1911	0.1911
		4	0.1904	0.1911	0.1911	0.1911	0.1911	0.1911
		5	0.1911	0.1911	0.1911	0.1911	0.1911	0.1911
	Analytic	0.1909...0.1915						
	dSV	2	0.0730	0.1079	0.1144	0.1147	0.1148	0.1148
		3	0.1077	0.1146	0.1148	0.1148	0.1148	0.1148
		4	0.1140	0.1147	0.1148	0.1148	0.1148	0.1148
		5	0.1148	0.1148	0.1148	0.1148	0.1148	0.1148
	Analytic	0.1148						
	W	2	0.1145	0.1138	0.1148	0.1148	0.1148	0.1148
		3	0.1098	0.1147	0.1148	0.1148	0.1148	0.1148
		4	0.1139	0.1148	0.1148	0.1148	0.1148	0.1148
		5	0.1148	0.1148	0.1148	0.1148	0.1148	0.1148
	Analytic	0.1147...0.1150						

shown in Table 2, LC3 (horizontal force, H) the solution is provided below; the same notation already used in [33] is adopted here, too. The reference solution for LC3 is:

$$\begin{aligned}
 u &= H(Rc_3(\cos \psi + \psi - 1) + (\psi c_1 - Rc_3)\sin \psi) , \\
 w &= H((\psi c_1 - Rc_3)\cos \psi + (c_2 - c_1 - Rc_3)\sin \psi + Rc_3) , \\
 \varphi &= Hc_3(1 - \psi - \cos \psi) .
 \end{aligned} \tag{22}$$

In Equation (22) u , w and φ are the tangential displacement, the radial displacement and the cross-section rotation, respectively, expressed in terms of the angle $\psi = s/R$, where s is the arc-length and R the curvature radius (see Section 2); for the sake of conciseness these compliance coefficients have been used:

$$c_1 = \frac{1}{2} \left(\frac{R}{EA} + \frac{R}{GA_T} + \frac{R^3}{EI} \right), \quad c_2 = \frac{R}{GA_T} + \frac{R^3}{EI}, \quad c_3 = \frac{R^2}{EI}, \tag{23}$$

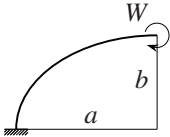
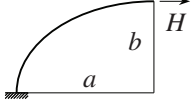
where A , A_T , I are respectively the cross section area, the shear area and the moment of inertia; E and G are the Young's modulus and the elastic shear modulus. Generalized stresses N , T and M assume the following values:

$$N = H \sin \psi, \quad T = H \cos \psi, \quad M = HR(\sin \psi - 1) . \tag{24}$$

A.2. Cantilever circular arch: Winkler's model. The analytical solution for the circular arch for the Winkler's approach, requires the definition of some sectional characteristics. The reduced moment of inertia is defined by:

$$I_r = \int_A \frac{y^2 R}{R - y} dA, \tag{25}$$

TABLE 9. Dimensionless radial tip deflection \hat{w} of a cantilever elliptical arch with $h \times t$ rectangular cross section and slenderness ratio $h/b = 1/5$ under bending couple $W = 1$ kNm or horizontal force $H = 1$ kN. Comparison between de Saint-Venant's (dSV) and Winkler's (W) solutions as functions of number of elements, n_e and NURBS order, p . Actual radial tip deflection w is related to the given one by Equation (21).

		p	n_e					
			2	4	8	16	32	64
	dSV	2	0.4280	0.5216	0.5306	0.5311	0.5312	0.5312
		3	0.5248	0.5310	0.5312	0.5312	0.5312	0.5312
		4	0.5309	0.5312	0.5312	0.5312	0.5312	0.5312
		5	0.5311	0.5312	0.5312	0.5312	0.5312	0.5312
		Analytic	0.5312					
	W	2	0.5162	0.5279	0.5287	0.5287	0.5287	0.5287
		3	0.5233	0.5286	0.5287	0.5287	0.5287	0.5287
		4	0.5284	0.5287	0.5287	0.5287	0.5287	0.5287
		5	0.5287	0.5287	0.5287	0.5287	0.5287	0.5287
		Analytic	0.5287...0.5314					
	dSV	2	0.2115	0.2436	0.2471	0.2473	0.2473	0.2473
		3	0.2443	0.2472	0.2473	0.2473	0.2473	0.2473
		4	0.2469	0.2473	0.2473	0.2473	0.2473	0.2473
		5	0.2473	0.2473	0.2473	0.2473	0.2473	0.2473
		Analytic	0.2473					
	W	2	0.2448	0.2464	0.2467	0.2467	0.2467	0.2467
		3	0.2445	0.2466	0.2467	0.2467	0.2467	0.2467
		4	0.2462	0.2466	0.2467	0.2467	0.2467	0.2467
		5	0.2467	0.2467	0.2467	0.2467	0.2467	0.2467
		Analytic	0.2455...0.2486					

where y is a coordinate measured along one of the principal inertia axis of the cross section. The reduced effective shear area is:

$$A_{Tr} = \left(\int_A \frac{R^2}{t^2(R-y)^2} \left(\frac{S_r}{I_r} - \frac{\Omega}{RA} \right)^2 dA \right)^{-1}, \quad (26)$$

where t is the cross section width, Ω is the portion of the cross section area lying below the value of y and S_r represents the reduced first moment of inertia referred to Ω :

$$S_r = \int_{\Omega} \frac{yR}{R-y} d\Omega, \quad (27)$$

A.2.1. *Load case 1, LC1.* In this case the analytical solution when a bending couple W (LC1) is acting at the free end is:

$$\begin{aligned} u &= W (c_3^* (\psi - \sin \psi) + c_1^* \psi), \\ w &= W c_3^* (1 - \cos \psi), \\ \varphi &= -W \frac{c_3^* + c_1^*}{R} \psi. \end{aligned} \quad (28)$$

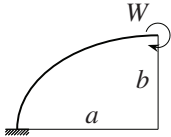
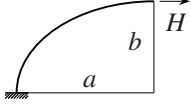
The same symbols already used for Equation (22) are adopted here, too. Compliance coefficients c_1^* , c_2^* and c_3^* are instead given by:

$$c_1^* = \frac{1}{EA}, \quad c_2^* = \frac{1}{2GA_{Tr}}, \quad c_3^* = \frac{R^2}{EI_r}. \quad (29)$$

Generalized stresses N , T and M assume the following values:

$$N = 0, \quad T = 0, \quad M = W. \quad (30)$$

TABLE 10. Dimensionless tangential tip displacement \hat{u} of a cantilever elliptical arch with $h \times t$ rectangular cross section and slenderness ratio $h/b = 1/5$ under bending couple $W = 1$ kNm or horizontal force $H = 1$ kN. Comparison between de Saint-Venant's (dSV) and Winkler's (W) solutions as functions of number of elements, n_e and NURBS order, p . Actual (dimensional) tangential tip deflection u is related to the given one by Equation (21)₂.

		n_e						
		p	2	4	8	16	32	64
	dSV	2	0.1638	0.1885	0.1909	0.1911	0.1911	0.1911
		3	0.1885	0.1910	0.1911	0.1911	0.1911	0.1911
		4	0.1909	0.1911	0.1911	0.1911	0.1911	0.1911
		5	0.1911	0.1911	0.1911	0.1911	0.1911	0.1911
	Analytic	0.1911						
	W	2	0.1905	0.1912	0.1914	0.1914	0.1914	0.1914
		3	0.1893	0.1913	0.1914	0.1914	0.1914	0.1914
		4	0.1912	0.1914	0.1914	0.1914	0.1914	0.1914
		5	0.1914	0.1914	0.1914	0.1914	0.1914	0.1914
	Analytic	0.1903...0.1927						
	dSV	2	0.1026	0.1154	0.1171	0.1172	0.1172	0.1172
		3	0.1152	0.1172	0.1172	0.1172	0.1172	0.1172
		4	0.1170	0.1172	0.1172	0.1172	0.1172	0.1172
		5	0.1172	0.1172	0.1172	0.1172	0.1172	0.1172
	Analytic	0.1172						
	W	2	0.1174	0.1171	0.1174	0.1174	0.1174	0.1174
		3	0.1160	0.1173	0.1174	0.1174	0.1174	0.1174
		4	0.1171	0.1174	0.1174	0.1174	0.1174	0.1174
		5	0.1174	0.1174	0.1174	0.1174	0.1174	0.1174
	Analytic	0.1169...0.1184						

A.2.2. *Load case 2, LC2.* The analytical solution for the circular arch under a vertical force P (LC2) acting at the free end is:

$$\begin{aligned}
 u &= \frac{1}{2}PR(c_3^* + 2c_2^*)(\sin \psi - \psi \cos \psi), \\
 w &= \frac{1}{2}PR(c_3^* + 2c_2^*)\psi \sin \psi, \\
 \varphi &= -Pc_3^* \sin \psi.
 \end{aligned} \tag{31}$$

The same definition of compliance coefficients given by Equation (29) applies here, too. Generalized stresses N , T and M assume in this case the following values:

$$N = -P \cos \psi, \quad T = P \sin \psi, \quad M = -PR \cos \psi. \tag{32}$$

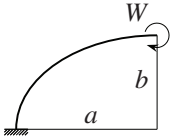
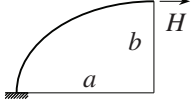
A.2.3. *Load case 3, LC3.* For the same circular arch, the analytical solution when a horizontal force H (LC3) acts at the free end is the following:

$$\begin{aligned}
 u &= HR \left((c_1^* + c_3^*)\psi - c_3^* + c_3^* \cos \psi - \left(c_3^* - \left(c_2^* + \frac{c_3^*}{2} \right) \psi \right) \sin \psi \right), \\
 w &= HR \left(c_3^* + \left(\left(c_2^* + \frac{c_3^*}{2} \right) \psi - c_3^* \right) \cos \psi + \left(c_2^* - \frac{c_3^*}{2} \right) \sin \psi \right), \\
 \varphi &= H \left(c_3^* - (c_1^* + c_3^*)\psi - c_3^* \cos \psi \right).
 \end{aligned} \tag{33}$$

Compliance coefficients c_1^* , c_2^* , c_3^* are again defined by Equation (29) while generalized stresses N , T and M assume now the following values:

$$N = H \sin \psi, \quad T = H \cos \psi, \quad M = HR (\sin \psi - 1). \tag{34}$$

TABLE 11. Dimensionless radial tip deflection \hat{w} of a cantilever elliptical arch with $h \times t$ rectangular cross section and slenderness ratio $h/b = 2/3$ under bending couple $W = 1$ kNm or horizontal force $H = 1$ kN. Comparison between de Saint-Venant's (dSV) and Winkler's (W) solutions as functions of number of elements, n_e and NURBS order, p . Actual radial tip deflection w is related to the given one by Equation (21)₁.

		n_e						
		p	2	4	8	16	32	64
	dSV	2	0.5185	0.5302	0.5311	0.5312	0.5312	0.5312
		3	0.5301	0.5312	0.5312	0.5312	0.5312	0.5312
		4	0.5312	0.5312	0.5312	0.5312	0.5312	0.5312
		5	0.5312	0.5312	0.5312	0.5312	0.5312	0.5312
		Analytic	0.5312					
	W	2	0.5024	0.5030	0.5030	0.5030	0.5030	0.5030
		3	0.5021	0.5030	0.5030	0.5030	0.5030	0.5030
		4	0.5030	0.5030	0.5030	0.5030	0.5030	0.5030
		5	0.5030	0.5030	0.5030	0.5030	0.5030	0.5030
		Analytic	0.4581...0.5334					
	dSV	2	0.2545	0.2584	0.2587	0.2587	0.2587	0.2587
		3	0.2583	0.2587	0.2587	0.2587	0.2587	0.2587
		4	0.2586	0.2587	0.2587	0.2587	0.2587	0.2587
		5	0.2587	0.2587	0.2587	0.2587	0.2587	0.2587
		Analytic	0.2587					
	W	2	0.2525	0.2524	0.2523	0.2523	0.2523	0.2523
		3	0.2522	0.2523	0.2523	0.2523	0.2523	0.2523
		4	0.2523	0.2523	0.2523	0.2523	0.2523	0.2523
		5	0.2523	0.2523	0.2523	0.2523	0.2523	0.2523
		Analytic	0.2376...0.2772					

A.3. **Circular chain ring.** The analytical solution of the circular chain ring (see Figure 10) under two opposite compressive forces, presented in Section 4.2 has been obtained integrating the governing differential equations: see Equation (2) and Equation (3) for both de Saint-Venant's and Winkler's models.

A.3.1. *de Saint-Venant's model.* For this case bending moment and axial force are given by:

$$M = PR \left(\frac{2}{\pi} - \cos \psi \right), \quad N = -P \cos \psi. \quad (35)$$

where R , P and ψ are shown in Figure 10.

Finally the normal stress expression is obtained by Navier's formula:

$$\sigma = \frac{N}{A} + \frac{M}{I} y, \quad (36)$$

where A is the cross section, I the moment of inertia and y is the position where the stress is evaluated.

A.3.2. *Winkler's model.* In this case the expressions of bending moment M and axial force N are:

$$M = PR \left(\frac{2AR^2}{\pi(AR^2 + I_r)} - \cos \psi \right), \quad N = -P \cos \psi. \quad (37)$$

where I_r is the reduced moment of inertia, defined above in Equation (25). While axial force is equal for both models, bending moment has a more complicated expression in this case. Also normal stress, which now takes into account the effect of the curvature has a more involved form:

$$\sigma = \frac{N}{A} - M \left(\frac{1}{RA} - \frac{Ry}{I_r(R-y)} \right). \quad (38)$$

TABLE 12. Dimensionless tangential tip displacement \hat{u} of a cantilever elliptical arch with $h \times t$ rectangular cross section and slenderness ratio $h/b = 2/3$ under bending couple $W = 1$ kNm or horizontal force $H = 1$ kN. Comparison between de Saint-Venant's (dSV) and Winkler's (W) solutions as functions of number of elements, n_e and NURBS order, p . Actual (dimensional) tangential tip deflection u is related to the given one by Equation (21)₂.

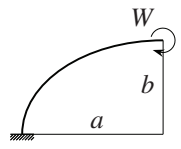
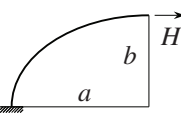
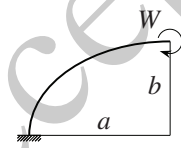
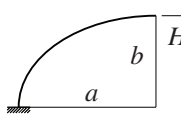
		n_e						
		p	2	4	8	16	32	64
	dSV	2	0.1883	0.1908	0.1910	0.1911	0.1911	0.1911
		3	0.1908	0.1911	0.1911	0.1911	0.1911	0.1911
		4	0.1910	0.1911	0.1911	0.1911	0.1911	0.1911
		5	0.1911	0.1911	0.1911	0.1911	0.1911	0.1911
		Analytic	0.1911					
	W	2	0.1950	0.1942	0.1941	0.1941	0.1941	0.1941
		3	0.1941	0.1941	0.1941	0.1941	0.1941	0.1941
		4	0.1941	0.1941	0.1941	0.1941	0.1941	0.1941
		5	0.1941	0.1941	0.1941	0.1941	0.1941	0.1941
		Analytic	0.1821 ... 0.2092					
	dSV	2	0.1490	0.1504	0.1506	0.1506	0.1506	0.1506
		3	0.1504	0.1506	0.1506	0.1506	0.1506	0.1506
		4	0.1505	0.1506	0.1506	0.1506	0.1506	0.1506
		5	0.1506	0.1506	0.1506	0.1506	0.1506	0.1506
		Analytic	0.1506					
	W	2	0.1548	0.1547	0.1547	0.1547	0.1547	0.1547
		3	0.1546	0.1547	0.1547	0.1547	0.1547	0.1547
		4	0.1547	0.1547	0.1547	0.1547	0.1547	0.1547
		5	0.1547	0.1547	0.1547	0.1547	0.1547	0.1547
		Analytic	0.1470 ... 0.1686					

TABLE 13. Cantilever elliptical arch: CPU time [s] spent by the codes implementing both de Saint-Venant's and Winkler's models as functions of NURBS order, p and number of elements, n_e .

		de Saint-Venant				Winkler				
		p								
		n_e	2	3	4	5	2	3	4	5
	2	0.178	0.178	0.179	0.179	0.188	0.191	0.194	0.194	
	4	0.178	0.178	0.179	0.181	0.190	0.193	0.194	0.194	
	8	0.179	0.181	0.182	0.181	0.192	0.193	0.196	0.196	
	16	0.181	0.183	0.186	0.190	0.194	0.197	0.197	0.202	
	32	0.187	0.188	0.195	0.199	0.196	0.204	0.208	0.213	
	64	0.195	0.201	0.212	0.221	0.207	0.220	0.229	0.237	
	2	0.177	0.178	0.178	0.179	0.185	0.185	0.185	0.189	
	4	0.177	0.177	0.180	0.182	0.185	0.185	0.186	0.189	
	8	0.180	0.180	0.180	0.185	0.186	0.186	0.188	0.192	
	16	0.181	0.182	0.187	0.188	0.189	0.189	0.194	0.198	
	32	0.189	0.191	0.195	0.201	0.194	0.196	0.203	0.206	
	64	0.199	0.206	0.212	0.222	0.205	0.212	0.224	0.238	

A.4. Elliptical chain ring. The analytical solution of the elliptical chain ring under two opposite tensile forces, see Figure 11, which was presented in Section 4.3, has been obtained by integrating the relevant governing equations. Ellipse geometry is described by semi-major axis, a and semi-minor axis, b ; once these are given, eccentricity, e , complementary eccentricity, e' and the ratio of

semi-axes, d , are defined as:

$$e = \sqrt{1 - \frac{b^2}{a^2}}, \quad e' = \sqrt{\frac{a^2}{b^2} - 1}, \quad d = \frac{b}{a} = \sqrt{1 - e^2}. \quad (39)$$

It can be easily checked, by using (39), that $e' = e/d$. Moreover the solution involves the complete elliptic integrals, of the first kind (see [72] and [73]):

$$K = K(k) = F\left(k, \frac{\pi}{2}\right) = \int_0^{\pi/2} \frac{d\theta}{\sqrt{1 - k^2 \sin^2 \theta}}, \quad (40)$$

and of the second kind (see [72] and [73]):

$$\bar{E} = \bar{E}(k) = E\left(k, \frac{\pi}{2}\right) = \int_0^{\pi/2} \sqrt{1 - k^2 \sin^2 \theta} d\theta, \quad (41)$$

where $F(k, \phi)$ and $E(k, \phi)$ are the incomplete elliptic integrals of the first and of the second kind, respectively, see [72].

In the sequel, taking into account that $k = e$, equations (40), (41) provide:

$$\bar{E} = \bar{E}(e) \quad K = K(e). \quad (42)$$

A.4.1. *de Saint-Venant's model.* Referring to Figure 11, the radial displacement at point A is:

$$w_A = \frac{Pa}{2e^2} \left((C_1 - C_2)Kd^2 + (C_2d^2 - C_1)\bar{E} + \frac{C_3d^2}{3} (Kd^2 - \bar{E}(e^2 + 1)) + \frac{3}{4\bar{E}} \left((\tan^{-1}e')^2 + 2de \tan^{-1}e' + d^2e^2 \right) \right) \quad (43)$$

The radial displacement at point B (see Figure 11) yields:

$$w_B = \frac{Pa}{2e^2} \left((C_2 - C_1)(d - d^2) + \frac{C_3d}{4\bar{E}} \left((de + \tan^{-1}e')(e + d^2 \tanh^{-1}e) - \frac{4\bar{E}}{3}(1 - d^3) \right) \right) \quad (44)$$

The compliance coefficients appearing in Equations (43) and (44) are defined in the following way:

$$C_1 = \frac{1}{EA}, \quad C_2 = \frac{1}{GA_T}, \quad C_3 = \frac{a^2}{EI}. \quad (45)$$

A.4.2. *Winkler's model.* The expression of the radial displacement at point A is:

$$w_A = \frac{Pa}{12e^2} \left(2C_1^* (d^2(e^2 + 8)K - d^2e\eta(d^2 - 1) - (d^2(2e^2 + 5) + 3)\bar{E}) + 6C_2^* d^2 (\bar{E} - K) + C_3^* d^2 \left(2d^2K - \frac{3d\eta}{2} (de + \tan^{-1}e') - 2(e^2 + 1)\bar{E} \right) \right), \quad (46)$$

where dimensionless coefficients λ , η , which are defined as:

$$\lambda = \frac{a^2A}{I_r} = \frac{C_3^*}{C_1^*}; \quad \eta = \frac{4e^3 - 3d^2e\lambda - 3d\lambda \tan^{-1}e'}{(d^2(3\lambda + 2) + 2)\bar{E} - d^2K}, \quad (47)$$

express the coupling between bending and axial force. For point B, the radial displacement is instead:

$$w_B = \frac{Pa}{24e^2} \left(\frac{4C_1^*}{1 + d^2} (d^4(2e^2 + e\eta + 7) - 2d^5 - 8d^3 + d^2(2e^4 + e^2 + 9) - 6d - e(\eta - 2e^3)) + 12C_2^* d(1 - d) + C_3^* d(4d^3 - 3d\eta(d^2 \tanh^{-1}e + e) - 4) \right). \quad (48)$$

In Equations (46) and (48) there appear compliance coefficients C_1^* , C_2^* and C_3^* , which are given by:

$$C_1^* = \frac{1}{EA}, \quad C_2^* = \frac{1}{GA_{Tr}}, \quad C_3^* = \frac{a^2}{EI_r}. \quad (49)$$

Coefficients C_1^* and C_3^* take into account axial and bending compliance (which are coupled in Winkler's model) while C_2^* is related to shear compliance; they are all functions of the curvature radius R .

Obviously in an ellipse, the curvature radius is variable; in this case the provided solution is an approximated one, since constant values of C_1^* , C_2^* , C_3^* have been considered when integrating the governing equations. In order to find upper and lower bound to the actual solution, the maximum and the minimum value of each coefficient have been computed and the corresponding minimum and maximum displacement have been obtained. This issue has been discussed detail in Section 4.3.

A.5. Cantilever elliptical arch. Also in this case the closed-form solution have been computed for both models and for the two considered loading conditions (LC1, bending couple W , and LC3, horizontal force H).

A.5.1. de Saint-Venant's model. For LC1, at free end, see Table 7, the radial (w) and tangential displacements (u) are:

$$\begin{aligned} w &= \frac{W}{2e} C_3 (e + d^2 \tanh^{-1} e), \\ u &= \frac{W}{2e} C_3 d (2\bar{E} e - de - \sin^{-1} e). \end{aligned} \quad (50)$$

The same procedure leads to the radial w and tangential u tip displacements under an horizontal force H (LC3) acting at the free end:

$$\begin{aligned} w &= \frac{Had}{e^2} \left((C_2 - C_1)(1 - d) + \frac{C_3 d^2}{6} (3e \tanh^{-1} e - 2(1 - d) + e^2) \right), \\ u &= \frac{Ha}{e^2} \left(C_1 (\bar{E} - d^2 K) + C_2 d^2 (K - \bar{E}) - \frac{C_3 d^2}{3} (d^2 K + 3e (de + \tan^{-1} e') - (4e^2 + 1) \bar{E}) \right). \end{aligned} \quad (51)$$

Geometry descriptors e , e' , d are the same appearing in Equation (39) (where a and b respectively are the semi-major and semi-minor axis of the ellipse), while compliance coefficients C_1 , C_2 , C_3 have been already defined in Equation (45).

A.5.2. Winkler's model. The solution of this problem by Winkler's models leads to a more complicated formulation with stiffness coefficients that vary with the curvature radius. The same procedure already outlined in Section A.4.2 has been adopted also in this case. Now the radial w and tangential tip displacements u for LC1 are:

$$\begin{aligned} w &= W \left(\frac{2C_1^* e^2}{3d^2} + \frac{C_3^*}{2e} (e + d^2 \tanh^{-1} e) \right), \\ u &= W \left(\frac{C_1^*}{3d} (2(d^2 + 1) \bar{E} + d(2e^2 - dK)) - \frac{C_3^* d}{2e} (de - 2e\bar{E} + \sin^{-1} e) \right) \end{aligned} \quad (52)$$

The same procedure leads to the the radial w and tangential u tip displacements due to a horizontal force H (LC3), acting at the free end, according to Winkler's constitutive model:

$$\begin{aligned} w &= \frac{Ha}{6de^2} (4C_1^* (4d - 3de^2 + 5e^2 - 4) + 6C_2^* d (d - d^2) + \\ &\quad - C_3^* d^2 (e^2 (2d - 3) - 3d^2 e \tanh^{-1} e - 2d + 2)) \\ u &= \frac{Ha}{3e^2} (C_1^* (4de^4 - (4e^4 - e^2 - 8) \bar{E} + 2(e^4 + 3e^2 - 4) K) - 3C_2^* d^2 (\bar{E} - K) + \\ &\quad - C_3^* d^2 (d^2 K + 3e (de + \sin^{-1} e) - (4e^2 + 1) \bar{E})) . \end{aligned} \quad (53)$$

ACKNOWLEDGEMENT

The financial support of MIUR, the Italian Ministry of University and Research , under grant number PRIN-2010MBJK5B. (Progetti di Ricerca di Interesse Nazionale bando 2012, Progetto *Dynamic, Stability and Control of Flexible Structures*) is gratefully acknowledged.

REFERENCES

- [1] T. J. R. Hughes, J. A. Cottrell, and Y. Bazilevs. Isogeometric analysis: CAD, finite elements, NURBS, exact geometry and mesh refinement. *Computer Methods in Applied Mechanics and Engineering*, 194:4135–4195, 2005.
- [2] J. A. Cottrell, T. J. R. Hughes, and Y. Bazilevs. *Isogeometric Analysis: Toward Integration of CAD and FEA*. Wiley, 2009.
- [3] T. J. R. Hughes, A. Reali, and G. Sangalli. Efficient quadrature for NURBS-based isogeometric analysis. *Computer Methods in Applied Mechanics and Engineering*, 199:301–313, 2010.
- [4] M. Aristodemo. A high continuity finite element model for two-dimensional elastic structures. *Computers and Structures*, 21:987–993, 1985.
- [5] A. Bilotta, G. Formica, and E. Turco. Performance of a high-continuity finite element in three-dimensional elasticity. *Communications in Numerical Methods in Engineering*, 26(9):1155–1175, 2010.
- [6] A. Benedetti and A. M. Tralli. A new hybrid F.E. model for arbitrarily curved beam—I. linear analysis. *Computers and Structures*, 33(6):1437–1449, 1989.
- [7] R. Echter and M. Bischoff. Numerical efficiency, locking and unlocking of NURBS finite elements. *Computer Methods in Applied Mechanics and Engineering*, 199(5–8):374–382, 2010.
- [8] M. Aristodemo and E. Turco. Boundary element discretization of plane elasticity and plate bending problems. *International Journal for Numerical Methods in Engineering*, 37:965–987, 1994.
- [9] E. Turco and M. Aristodemo. A three-dimensional B-spline boundary element. *Computer Methods in Applied Mechanics and Engineering*, 155:119–128, 1998.
- [10] D. J. Benson, Y. Bazilevs, M. C. Hsu, and T. J. R. Hughes. Isogeometric shell analysis: the Reissner-Mindlin shell. *Computer Methods in Applied Mechanics and Engineering*, 199:276–289, 2010.
- [11] F. Auricchio, L. Beirão da Veiga, T. J. R. Hughes, A. Reali, and G. Sangalli. Isogeometric collocation for elastostatics and explicit dynamics. *Computer Methods in Applied Mechanics and Engineering*, 249-252:2–14, 2012.
- [12] F. Auricchio, L. Beirão da Veiga, J. Kiendl, C. Lovadina, and A. Reali. Locking-free isogeometric collocation methods for spatial Timoshenko rods. *Computer Methods in Applied Mechanics and Engineering*, 263:113–126, 2013.
- [13] R. Bouclier, T. Elguedj, and A. Combescure. Locking free isogeometric formulations of curved thick beams. *Computer Methods in Applied Mechanics and Engineering*, 245-246:144–162, 2012.
- [14] L. Greco and M. Cuomo. B-Spline interpolation of Kirchhoff-Love space rods. *Computer Methods in Applied Mechanics and Engineering*, 256:251–269, 2013.
- [15] L. Greco and M. Cuomo. An implicit G^1 multi patch B-spline interpolation for Kirchhoff-Love space rod. *Computer Methods in Applied Mechanics and Engineering*, 269:173–197, 2014.
- [16] L. Beirão da Veiga, C. Lovadina, and A. Reali. Avoiding shear locking for the Timoshenko beam problem via isogeometric collocation methods. *Computer Methods in Applied Mechanics and Engineering*, 241-244:38–51, 2012.
- [17] E. Winkler. Formänderung und Festigkeit gekrümmter Körper, insbesondere der Ringe. *Der Civilingenieur*, 4:232–246, 1858.
- [18] V. L. Berdichevskii and L. A. Starosel'skii. On the theory of curvilinear Timoshenko-type rods. *Journal of Applied Mathematics and Mechanics*, 47(6):809–817, 1983.
- [19] W. Yu, D.H. Hodges, V. Volovoi, and C. E. S. Cesnik. On Timoshenko-like modeling of initially curved and twisted composite beams. *International Journal of Solids and Structures*, 39:5101–5121, 2002.
- [20] W. Yu and D. H. Hodges. Generalized timoshenko theory of the variational asymptotic beam sectional analysis. *Journal of the American Helicopter Society*, 50(1):46–55, January 2005.

- [21] W. Yu and D. H. Hodges. Elasticity solutions versus asymptotic sectional analysis of homogeneous, isotropic, prismatic beams. *Journal of Applied Mechanics*, 71:15–23, January 2004.
- [22] M. Borri, G. L. Ghiringhelli, and T. Merlini. Linear analysis of naturally curved and twisted beams. *Composites Engineering*, 2(5-7):433–456, 1992.
- [23] V. Giavotto, M. Borri, P. Mantegazza, G. Ghiringhelli, V. Carmaschi, G. C. Maffioli, and F. Mussi. Anisotropic beam theory and applications. *Computers and Structures*, 16(1-4):403–413, 1983.
- [24] M. Morandini, M. Chierichetti, and P. Mantegazza. Characteristic behavior of prismatic anisotropic beam via generalized eigenvectors. *International Journal of Solids and Structures*, 47:1327–1337, 2010.
- [25] M. Borri and C. Bottasso. An Intrinsic Beam Model Based on a Helicoidal Approximation – Part I: Formulation. *International Journal for Numerical Methods in Engineering*, 37:2267–2289, 1994.
- [26] M. Borri and C. Bottasso. An Intrinsic Beam Model Based on a Helicoidal Approximation – Part II: Linearization and Finite Element Implementation. *International Journal for Numerical Methods in Engineering*, 37:2291–2309, 1994.
- [27] S. P. Timoshenko and J. N. Goodier. *Theory of Elasticity*. McGraw-Hill International, 3-rd edition, 1982.
- [28] E. E. Webel. Studies in Photoelasticity Stress Determination. *Transactions of the American Society of Mechanical Engineers*, 56:637–658, 1931.
- [29] H. Resal. Formules pour le calcul de la résistance des chaînes à mailles plats. *Annales des Mines*, 1(ser. VI): 617–630, 1862.
- [30] J. T. Oden. *Mechanics of Elastic Structures*. McGraw-Hill, 1967.
- [31] L. Piegl and W. Tiller. *The NURBS Book*. Springer, 2nd edition, 1997.
- [32] M. P. do Carmo. *Differential Geometries of Curves and Surfaces*. Prentice-Hall, 1976.
- [33] A. Cazzani, M. Malagù, and E. Turco. Isogeometric analysis of plane curved beams. *Mathematics and Mechanics of Solids*, 1081286514531265, first published on April 20, 2014 doi:10.1177/1081286514531265, 2014.
- [34] O. Belluzzi. *Scienza delle Costruzioni*, volume 2 (In italian). Zanichelli, 1942.
- [35] K. C. Lin and S. H. Huang. Static closed-form solutions for in-plane shear deformable curved beams with variable curvatures. *Journal of Solid Mechanics and Materials Engineering*, 1(11):1362–1373, 2007.
- [36] K. C. Lin and S. H. Huang. Static closed-form solutions for in-plane thick curved beams with variable curvatures. *Journal of Solid Mechanics and Materials Engineering*, 1(8):1026–1034, 2007.
- [37] A. Cazzani, M. Malagù, and E. Turco. Isogeometric analysis: A powerful numerical tool for the elastic analysis of historical masonry arches. *Continuum Mechanics and Thermodynamics*, (submitted), 2014.
- [38] M. Pignataro and A. Luongo. Asymmetric interactive buckling of thin-walled columns with initial imperfections. *Thin-Walled Structures*, 5(5):365–382, 1987.
- [39] A. Luongo. Mode localization in dynamics and buckling of linear imperfect continuous structures. *Nonlinear Dynamics*, 25(1-3):133–156, 2001.
- [40] A. Luongo. On the amplitude modulation and localization phenomena in interactive buckling problems. *International Journal of Solids and Structures*, 27(15):1943–1954, 1991.
- [41] M. Pignataro, A. Luongo, and N. Rizzi. On the effect of the local overall interaction on the postbuckling of uniformly compressed channels. *Thin-Walled Structures*, 3(4):293–321, 1985.
- [42] J. A. Cottrell, A. Reali, Y. Bazilevs, and T. J. R. Hughes. Isogeometric analysis of structural vibrations. *Computer Methods in Applied Mechanics and Engineering*, 195:5257–5296, 2006.
- [43] S. N. Atluri and A. Cazzani. Rotations in computational solid mechanics. *Archives of Computational Methods in Engineering*, 2:49–138, 1995.
- [44] A. Cazzani and S. N. Atluri. Four-noded mixed finite elements, using unsymmetric stresses, for linear analysis of membranes. *Computational Mechanics*, 11:229–251, 1993.

- [45] A. Cazzani and C. Lovadina. On some mixed finite element methods for plane membrane problems. *Computational Mechanics*, 20:560–572, 1997.
- [46] A. Cazzani, E. Garusi, A. Tralli, and S. N. Atluri. A four-node hybrid assumed-strain finite element for laminated composite plates. *Computers, Materials & Continua*, 2:23–38, 2005.
- [47] A. Rinaldi and L. Placidi. A microscale second gradient approximation of the damage parameter of quasi-brittle heterogeneous lattices. *ZAMM - Zeitschrift für Angewandte Mathematik und Mechanik*, 1(16):DOI 10.1002/zamm.201300028, 2013.
- [48] A. Rinaldi. A rational model for 2D disordered lattices under uniaxial loading. *International Journal of Damage Mechanics*, 18:233–257, 2009.
- [49] A. Rinaldi. Statistical model with two order parameters for ductile and statistical model with two order parameters for ductile and soft fiber bundles in nanoscience and biomaterials. *Physical Review E (Statistical, Nonlinear, and Soft Matter Physics)*, 83(046126(10)), 2011.
- [50] V. A. Eremeyev and W. Pietraszkiewicz. The nonlinear theory of elastic shells with phase transitions. *Journal of Elasticity*, 74(1):67–86, 2004.
- [51] V. A. Eremeyev, A. B. Freidin, and L. L. Sharipova. The stability of the equilibrium of two-phase elastic solids. *Journal of Applied Mathematics and Mechanics*, 71(1):61–84, 2007.
- [52] V. A. Eremeyev, A. B. Freidin, and L. L. Sharipova. Nonuniqueness and stability in problems of equilibrium of elastic two-phase bodies. *Doklady Physics*, 48(7):359–363, 2003.
- [53] F. dell’Isola and A. Romano. On the derivation of thermomechanical balance equations for continuous systems with a nonmaterial interface. *International Journal of Engineering Science*, 25(11-12):1459–1468, 1987.
- [54] F. D’Annibale and A. Luongo. A damage constitutive model for sliding friction coupled to wear. *Continuum Mechanics and Thermodynamics*, 25(2-4):503–522, 2013.
- [55] F. dell’Isola, A. Madeo, and P. Seppecher. Boundary conditions at fluid-permeable interfaces in porous media: A variational approach. *International Journal of Solids and Structures*, 46(17):3150–3164, 2009.
- [56] F. dell’Isola, P. Seppecher, and A. Madeo. How contact interactions may depend on the shape of cauchy cuts in n-th gradient continua: approach á la D’Alembert. *Zeitschrift für Angewandte Mathematik und Physik (ZAMP)*, 63(6):1119–1141, 2012.
- [57] F. dell’Isola and P. Seppecher. The relationship between edge contact forces, double forces and interstitial working allowed by the principle of virtual power. *Comptes Rendus de l’Academie de Sciences - Serie IIB: Mecanique, Physique, Chimie, Astronomie*, 321:303–308, 1995.
- [58] S. Federico, A. Grillo, S. Imatani, G. Giaquinta, and W. Herzog. An energetic approach to the analysis of anisotropic hyperelastic materials. *International Journal of Engineering Science*, 46:164–181, 2008.
- [59] A. Misra. Mechanistic model for contact between rough surfaces. *Journal of Engineering mechanics*, 123(5):475–484, 1997.
- [60] N. Roveri and A. Carcaterra. Damage detection in structures under travelling loads by the Hilbert-Huang transform. *Mechanical System and Signal Processing*, 28:128–144, 2012.
- [61] M. Ferretti and G. Piccardo. Dynamic modeling of taut strings carrying a traveling mass. *Continuum Mechanics and Thermodynamics*, 25(2-4):469–488, 2013.
- [62] E. Turco. Load distribution modelling for pin-jointed trusses by an inverse approach. *Computer Methods in Applied Mechanics and Engineering*, 165:291–306, 1998.
- [63] E. Turco. A strategy to identify exciting forces acting on structures. *International Journal for Numerical Methods in Engineering*, 64:1483–1508, 2005.
- [64] E. Turco. Is the statistical approach suitable for identifying actions on structures? *Computers and Structures*, 83:2112–2120, 2005.
- [65] E. Turco. Identification of axial forces on statically indeterminate pin-jointed trusses by a nondestructive mechanical test. *The Open Civil Engineering Journal*, 7:50–57, 2013.
- [66] R. Contro, C. Poggi, and A. Cazzani. Numerical analysis of fire effects on beam structures. *Engineering Computations*, 5:53–58, 1988.
- [67] A. Cazzani, R. Contro, and L. Corradi. On the evaluation of the shakedown boundary for temperature-dependent elastic properties. *European Journal of Mechanics A/Solids*, 11:539–550, 1992.

- [68] U. Andreaus and P. Baragatti. Cracked beam identification by numerically analysing the nonlinear behaviour of the harmonically forced response. *Journal of Sound and Vibration*, 330(4):721–742, 2011.
- [69] A. Cazzani and M. Rovati. Sensitivity analysis and optimum design of elastic-plastic structural systems. *Meccanica*, 26:173–178, 1991.
- [70] E. Turco and P. Caracciolo. Elasto-plastic analysis of Kirchhoff plates by high simplicity finite elements. *Computer Methods in Applied Mechanics and Engineering*, 190:691–706, 2000.
- [71] P. Neff, A. Sysow, and C. Wieners. Numerical approximation of incremental infinitesimal gradient plasticity. *International Journal for Numerical Methods in Engineering*, 77:414–436, 2009.
- [72] M. R. Spiegel, S. Lipschutz, and J. Liu. *Mathematical Handbook of Formulas and Tables*. McGraw–Hill, Third edition, 2009.
- [73] G. A. Korn and T. M. Korn. *Mathematical Handbook for Scientist and Engineers*. Dover Publications, 2000.

DICAAR, UNIVERSITÀ DEGLI STUDI DI CAGLIARI, ANTONIO.CAZZANI@UNICA.IT

DICAAR, UNIVERSITÀ DEGLI STUDI DI CAGLIARI, MARCELLO.MALAGU@GMAIL.COM

DADU, UNIVERSITÀ DI SASSARI, FSTOCHINO@UNISS.IT

DADU, UNIVERSITÀ DI SASSARI, EMILIO.TURCO@UNISS.IT

Accepted Manuscript